Journal of Zhejiang University-SCIENCE A
www.jzus.zju.edu.cn; www.springer.com/journal/11582
E-mail: jzus_a@zju.edu.cn

Research Article
https://doi.org/10.1631/jzus.A2500461

Model for predicting the state of health of redox flow batteries based on an extreme learning machine model and swarm intelligence algorithm

Lei ZHANG[1,2], Zebo HUANG[3], Guo'an YANG[2], Fengming CHU[1,2]✉

[1]*Beijing Key Laboratory of Heat Transfer and Energy Conversion, College of Mechanical and Energy Engineering, Beijing University of Technology, Beijing 100124, China*
[2]*College of Mechanical and Electrical Engineering, Beijing University of Chemical Technology, Beijing 100029, China*
[3]*School of Mechanical and Electrical Engineering, Guilin University of Electronic Technology, Guilin 541214, China*

Abstract: Accurate assessment of the state of health (SOH) is essential for the safe, economical, and reliable operation of all-vanadium redox flow batteries (VRFBs). However, systems for monitoring their SOH have rarely been studied. In this study, capacity retention rate is used to characterize the SOH, and a series of charging/discharging cycling tests is conducted. Based on a series of operational parameters and grey relation analysis (GRA), the best health feature subset to characterize the SOH is determined. Extreme learning machine (ELM) combined with swarm intelligence algorithms is used to predict SOH, based on which the effects of different swarm intelligence algorithms and different activation functions on estimations of SOH performance are investigated. Results show that all the models with poor prediction results have a sigmoid activation function, indicating that such functions are not capable of predicting SOH. Grey relational analysis based on the LASSO (LGRA) algorithm-ELM is more suitable for SOH prediction than the interaction measurement algorithm based on Spearman's correlation coefficient (SCIM) algorithm-ELM model (here, LASSO is the least absolute shrinkage and selection operator). It can not only estimate SOH accurately but also predict recession characteristics. The most suitable swarm intelligence algorithm is particle swarm optimization (PSO), and the best activation function is linear, in which the maximum error is lower than 0.2%.

Key words: Group intelligence algorithm; Health feature subset; Spearman coefficient; Robustness; Interaction measure algorithm

1 Introduction

With the continuous development of science and technology, both the use and demand for energy have increased significantly in recent decades. However, the overuse of fossil fuels can result in excessive carbon dioxide emissions and global warming. The development of renewable and clean energy is one of the most effective technologies to address this problem. The intermittent and unstable supply of renewable energy, including wind and solar power, is a main issue for the grid (Guo et al., 2023). Large-scale and safe energy storage devices are needed to overcome these constraints. All-vanadium redox flow batteries (VRFBs) are regarded as one of the most promising energy storage technologies for clean energy systems, owing to their flexible structure, high safety, and long service life (Tan et al., 2017). The use of VRFBs can improve the stability of the grid and electrical power systems.

In recent years, many studies on redox flow batteries have been carried out on aspects such as flow field optimization, electrode and membrane design, and catalyst development. Battery capacity degradation and functional failure in commercial operation also deserve close attention. The real-time fault and state of health (SOH) monitoring of redox flow batteries is a key research field aiming to improve battery performance and efficiency (Ren et al., 2022; Yu et al., 2022). However, studies of methods for predicting the SOH of redox flow batteries are rare. Most studies of SOH prediction of electrochemical energy storage have been on lithium-ion batteries. Some researchers

✉ Fengming CHU, chufm@bjut.edu.cn
Fengming CHU, https://orcid.org/0009-0003-2083-4264

Received Sept. 19, 2025; Revision accepted Jan. 13, 2026; Crosschecked Mar. 24, 2026

© Zhejiang University Press 2026

proposed a data-driven approach, with no need for a complex electrochemical reaction model. A data-driven approach can use machine learning and other techniques to build linear or nonlinear prediction models to estimate the SOH based on a mass of experimental data. Shen et al. (2019) used a deep learning technique and combined a deep convolutional neural network to predict the charging capacity of a lithium-ion battery based on voltage, current, and partial charging cycles. Their method can accurately measure battery capacity online during the charging period with superior robustness and accuracy compared to other methods. Zhang et al. (2019) proposed a method based on the combination of a capacity increment and an artificial neural network for estimating the remaining life of a lithium-ion battery under constant-current discharging. They carried out correlation analysis to find highly correlated parameters and established a neural network model to predict SOH and remaining life. After training and validation, results show that this method has high accuracy and reliability. Chang et al. (2021) established a data-driven approach to estimate the remaining life of lithium-ion batteries, which combines a genetic algorithm, incremental capacity, and a wavelet neural network to extract relevant health features. Many relevant experiments conducted for training and validation show that the SOH estimation error is less than 3%, without considering the effect of temperature. Meng JH et al. (2018) adopted an image segmentation method based on a support vector machine (SVM) to extract the feature value types related to SOH by measuring the voltage response. This produces a mass of data types, from which those with the strongest correlation with SOH can be extracted. This method can accurately predict the SOH of a lithium iron phosphate battery by using the SVM. The main advantage of this method is that the feature extraction process is simple. Patil et al. (2015) proposed a coupling model combining the multilayer SVM and regression algorithms, based on which the remaining life of a lithium-ion battery can be predicted accurately. Sui et al. (2021) conducted a comprehensive comparison of SOH estimation methods based on machine learning, taking the performance of the algorithm and many factors of feature extraction into account. They reported that the SVM and artificial neural network are the most deeply studied SOH estimation methods. Lin et al. (2025) established a machine learning method based on physical information for SOH prediction of lithium-ion batteries, based on which the average error is 0.84% and the minimum error is 0.02%. Using their method, the physical aging information of the battery is extracted by a fractional-order equivalent circuit model, which is used as the data basis. Wei et al. (2018) proposed an autoregressive exogenous model integrated with a genetic algorithm and recursive least squares, which can simulate the dynamic behavior of VRFBs. The SOH can be estimated with excellent fast convergence, prediction accuracy, and robustness under uncertain initial states, electrolyte imbalance, and system performance conditions. Li PH et al. (2020) proposed a multi-cell shared prediction framework and designed a long short-term memory (LSTM) neural network model, which can select historical input data and new data simultaneously. After element-wise multiplication, the most useful information for SOH and remaining useful life (RUL) estimation can be filtered out. The SOH and RUL can be estimated accurately, with an average root mean square (RMS) of 0.0216 for SOH and 0.0831 for RUL, respectively. All the above methods are data-driven, with excellent robustness and adaptability. The data-driven approaches can be combined with optimization algorithms, leading to excellent and fast prediction results.

On the other hand, many scholars used a physical model-driven approach to predict SOH. This approach can describe the internal chemical dynamics by establishing mathematical models with physical interpretability. The physical model-driven approach does not need a large amount of data, which further enhances its physical interpretability. Calborean et al. (2020) used electrochemical impedance spectra to monitor the aging of lead-acid batteries and established an accurate mathematical fitting model to predict the aging process and remaining life of lead-acid batteries. Struckmann et al. (2020) developed a physical model for SOH to explain the internal chemical behavior of vanadium redox flow batteries using Nernst's equation and an in-situ model based on the Coulomb integral method. However, this in-situ monitoring method is for half cells. Wang LM et al. (2017) compared the advantages and disadvantages of cyclic voltammetry and differential pressure analysis in SOH prediction. They established a lithium iron phosphate battery model using an equivalent circuit model based on a local data symmetry method, which proves to be effective. Li S et al. (2020) proposed an online method

for estimating SOH based on an open-circuit voltage approach, which is used to predict SOH at the positive and negative electrodes of vanadium redox flow batteries. An SOH indicator derived from the capacity estimation can indicate the need for maintenance or repair. Li J et al. (2018) captured the formation process of the solid electrolyte interphase (SEI) layer in a single-particle model. By coupling a lithium-ion loss model induced via SEI formation with an advanced single-particle model that incorporates electrolyte physics, rapid prediction of capacity degradation and voltage curve evolution can be achieved. Huang et al. (2025) used the voltage response of the battery under a predefined current excitation at the beginning of life (BOL) as a reference to compensate for modeling uncertainties. By applying the same excitation during operation and comparing the generated voltage response with the BOL trajectory, key health-related parameters can be accurately estimated. In addition, many researchers have achieved accurate SOH or RUL prediction by combining physics-based models with data-driven approaches. For example, physical information or equivalent circuit models (ECMs) can be embedded in neural networks to enhance prediction accuracy and model interpretability (Wang FJ et al., 2024; Sun et al., 2025; Gu et al., 2026). Feng et al. (2025) comprehensively discussed the main factors affecting the accuracy of SOC estimation. Meng X et al. (2025b) developed a simplified model for proton exchange membrane fuel cells by considering concentration and ohmic losses, in which the open-circuit voltage is used to enable online estimation of the SOH, achieving high prediction accuracy. Subsequently, they developed a novel model to overcome the limitations imposed by the recovery mechanism of fuel cells, significantly enhancing the model's realism and practical applicability (Meng X et al., 2025a; Chu et al., 2026).

Those studies focus on estimating the SOH of lithium-ion or lead-acid batteries. Only two studies on redox flow batteries are reported, both of which are based on the physical model-driven approach (Ge et al., 2021; Yao et al., 2021; Zhao et al., 2023; Lei et al., 2024; Gong et al., 2025). Building a rapid real-time prediction model for redox flow batteries is needed urgently. In this paper, the performance of different health feature subsets in predicting SOH is investigated, and the analytical methods of grey correlation analysis and interaction measure are compared, based on which a data-driven approach of extreme learning machine (ELM) is established. A swarm intelligence algorithm is applied to optimize the connection weights of the ELM input layer and the thresholds of the hidden layer to enhance prediction accuracy. Based on the predicting error parameters, the estimation performance of different swarm intelligence algorithms combined with various activation functions is investigated, and the method yielding the lowest error is identified.

2 SOH prediction model

2.1 Definition of SOH

SOH is a crucial indicator that can reflect the performance and longevity of a redox flow battery. It is significantly affected by the multiple physical parameters, including the battery capacity, power output, internal resistance, cycle number, and energy efficiency. Although extensive studies have been conducted on estimation of the SOH lithium-ion batteries, a standardized definition of SOH for redox flow batteries has yet to be established. A physical parameter that shows a strong correlation with SOH can be regarded as a health characteristic. Among these, capacity plays a key role in redox flow battery performance. Consequently, in this study we select capacity as the representative indicator for SOH evaluation. Capacity-based SOH characterization can be described by the following equation:

$$S_{\mathrm{HC}} = \frac{C_{\mathrm{present}}}{C_{\mathrm{new}}} \times 100\%, \tag{1}$$

where S_{HC} denotes the SOH based on capacity characterization, C_{present} (kWh) is the remaining capacity, and C_{new} (kWh) represents the rated capacity of the new battery.

2.2 Health feature subset

To obtain the accurate SOH of a VRFB, the first step is to determine the most appropriate subset of health features by conducting charge–discharge cycling tests. The relationship between these parameters and SOH is complex, and too many parameters are involved in redox flow battery operation, including charging/discharging capacity, charge/discharge efficiency, charging energy, capacity retention rate, charging direct

current (DC) internal resistance, discharging DC internal resistance, and energy efficiency. Determining a suitable subset of health features can not only reduce computational overhead but also increase prediction accuracy. A series of charge–discharge cycling experiments is carried out, and a model for analyzing the impact of interacting parameters is established. The battery used in our experiments is the ZSHG-FUEL-22 with a bolt type single battery fixture, produced by the Wuhan Zhisheng New Energy Co., Ltd., China. The experimental procedures, equipment specifications, and correlation analysis methods involved in this study are described in detail in the electronic supplementary materials (ESM).

2.3 Extreme learning machine

SVM, back propagation (BP), and LSTM networks are widely used algorithms for state prediction. Compared to these algorithms, ELM stands out due to its high prediction accuracy, fast convergence speed, strong generalization capability, and suitability for modeling diverse data types (Chen et al., 2024).

In this work, ELM was used as the main algorithm for SOH prediction of a redox flow battery for the first time. An intelligent prediction model based on ELM is established. The ELM is a learning algorithm designed for single-hidden-layer feedforward neural networks (SLFNs).

The ELM model (Fig. 1) consists of three layers: an input layer, hidden layer, and output layer. In the input layer, each node corresponds to a feature variable, and the number of nodes is determined by the dimensionality of the input data. Each input node is fully connected to all neurons in the hidden layer via weighted links. The number of hidden neurons can be specified depending on the complexity of the task. Input signals are transformed in the hidden layer by applying a nonlinear activation function to the weighted sum of the inputs plus a bias term. Notably, the input weights and biases are randomly initialized and remain fixed during training. The output layer receives the nonlinear feature representations from the hidden layer and produces the final prediction through linear combination.

The activation function plays a pivotal role in the ELM, as it governs the network's capacity to model nonlinear patterns. By introducing nonlinear transformations to the input data, the activation function enables the ELM to approximate complex relationships

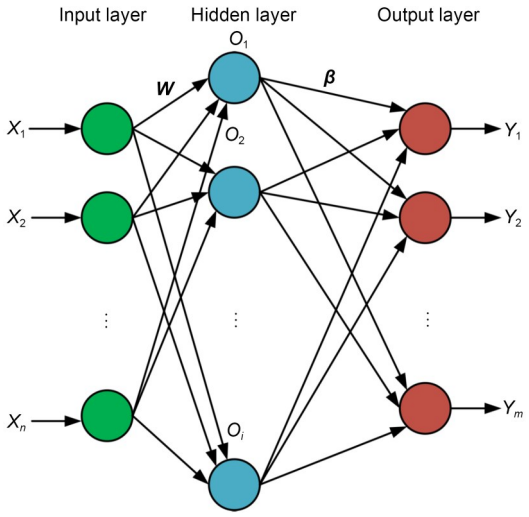


Fig. 1 Structure of the ELM model. X_n denotes the nth input feature. The hidden layer output is represented by O_i, which corresponds to the output of the ith hidden neuron after activation. Y_m is the mth output of the network. W is the input weight matrix connecting the input layer to the hidden layer, while β is the output weight matrix connecting the hidden layer to the output layer

between inputs and outputs. This mechanism is fundamental to enhancing the model's representational power and improving its generalization performance. In this study, four activation functions are selected: rectified linear unit (ReLU), linear, tanh, and sigmoid. The compatibility of the different activation functions with ELM is investigated by comparing their performance in SOH prediction.

2.4 Optimal strategy based on swarm intelligence

Although the ELM offers obvious advantages such as fast training speed and a simple network structure, it suffers from a critical limitation. The input weights and biases between the input and hidden layers are initialized randomly and fixed throughout the training process. This inherent randomness may lead to instability across different runs, and may result in suboptimal prediction. Additionally, ELM is highly sensitive to its initial parameters and lacks a self-adjustment mechanism for parameter optimization. To address these issues, swarm intelligence algorithms are used to enhance the stability and predictive accuracy of the ELM model both in the regression and classification tasks. Swarm intelligence algorithms are characterized by their strong global search ability and capacity to escape local optima. The integration of swarm intelligence algorithms with ELM can explore the

complex parameter space and identify the optimal set of input weights and biases effectively. In this study, four optimization algorithms, namely the sand cat swarm optimization (SCSO), particle swarm optimization (PSO), dung beetle optimization (DBO), and ant colony optimization (ACO), are used to optimize the ELM model and improve its overall performance.

2.5 Model parameters

Based on the SCIM (interaction measurement algorithm based on Spearman's correlation coefficient) and LGRA (grey relational analysis based on the least absolute shrinkage and selection operator) analysis, the four swarm intelligence algorithms and four activation functions are combined, resulting in 32 algorithm models for all possible combinations. To evaluate the prediction performance of the 32 algorithm models, four indicators are used: the mean absolute error (MAE, E_{MA}), mean square error (MSE, E_{MS}), mean absolute percentage error (MAPE, E_{MAP}), and coefficient of determination (R^2). MAE represents the average level of deviation between the predicted SOH and true SOH. A smaller value of MAE means a smaller deviation between the predicted value and true value. MSE represents the square of the error between the predicted and true values, and is more sensitive to outliers. MSE is used to confirm whether there is a large error in the sample. When there is a large error in the sample, MSE will increase dramatically. MAPE is a widely used parameter for evaluating the accuracy of regression models. It can present the average magnitude of errors between the predicted and actual values, expressed as a percentage of the actual values. MAPE can provide a relative measure of error, which is particularly useful when the scale of the data varies or when comparisons across different datasets are needed. R^2 reflects the degree of fit between the predicted values and real values. When R^2=1, the real values fit perfectly with the predicted values. When 0< R^2<1, it indicates that the model has some explanatory power and fits the data better than using the mean as a predictor, though there is still room for improvement. When R^2<0, it indicates that the model's fit is very poor—worse than simply using the mean value as a predictor. These four performance evaluation indexes can specifically and comprehensively evaluate the overall performance of the model, and more intuitively reflect its overall stability and prediction accuracy.

$$E_{\mathrm{MA}}=\frac{1}{n}\sum_{i=1}^{n}|y_i-\hat{y}_i|, \tag{2}$$

$$E_{\mathrm{MS}}=\frac{1}{n}\sum_{i=1}^{n}(y_i-\hat{y}_i)^2, \tag{3}$$

$$R^2=1-\frac{\sum_{i=1}^{n}(y_i-\hat{y}_i)^2}{\sum_{i=1}^{n}(y_i-\bar{y}_i)^2}, \tag{4}$$

$$E_{\mathrm{MAP}}=\frac{1}{n}\sum_{i=1}^{n}\left|\frac{y_i-\hat{y}_i}{y_i}\right|\times 100\%, \tag{5}$$

where y_i represents the true value of the SOH, $\hat{y}_i$ is the predicted value, n represents the number of samples, and $\bar{y}_i$ represents the mean of all real SOHs. R^2 is used to measure the degree, to which the model explains the variance of the data, reflecting the degree of fit between the predicted values and real values.

To compare the prediction performance of the 32 model algorithms, the parameters of ELM are kept constant. The swarm size of the swarm intelligence algorithms is also kept the same. The specific parameter settings are shown in Table 1.

Table 1 Specific parameters of the swarm intelligence algorithm combined with the ELM model

Parameter	Description
Population size	200
Maximum number of iterations	3000
Number of hidden neurons in ELM	200
ELM regularization coefficient, λ	0.1
Activation function	ReLU, linear, sigmoid, and tanh
ELM smoothing factor, β	0.9

3 Results and discussion

3.1 Correlation analysis

For testing the SCIM algorithm, the discharging capacity, charging energy, charging capacity, discharging DC internal resistance, energy efficiency, charging and discharging efficiency, are defined as x_1–x_6 (Table 2). The top 20 candidate subsets are filtered out based on the degree of correlation between each physical parameter and the SOH, and are ranked in Table 3.

The correlations of the health feature subsets are shown in Fig. 2, in which the Z-axis represents the

Table 2 Input variables used by SCIM

Input variable	X
Discharging capacity	x_1
Charging energy	x_2
Charging capacity	x_3
Discharging DC internal resistance	x_4
Energy efficiency	x_5
Charging and discharging efficiency	x_6

Table 3 Health feature subsets selected by SCIM

No.	Subset	No.	Subset
1	$\{x_1\}$	11	$\{x_2, x_3, x_4\}$
2	$\{x_1, x_2\}$	12	$\{x_1, x_4\}$
3	$\{x_1, x_3\}$	13	$\{x_2, x_4\}$
4	$\{x_1, x_2, x_3\}$	14	$\{x_3, x_4\}$
5	$\{x_2\}$	15	$\{x_4\}$
6	$\{x_3\}$	16	$\{x_1, x_2, x_3, x_4, x_5\}$
7	$\{x_2, x_3\}$	17	$\{x_1, x_2, x_3, x_4, x_6\}$
8	$\{x_1, x_2, x_3, x_4\}$	18	$\{x_1, x_2, x_3, x_5\}$
9	$\{x_1, x_2, x_4\}$	19	$\{x_1, x_2, x_4, x_5\}$
10	$\{x_1, x_3, x_4\}$	20	$\{x_1, x_3, x_4, x_5\}$

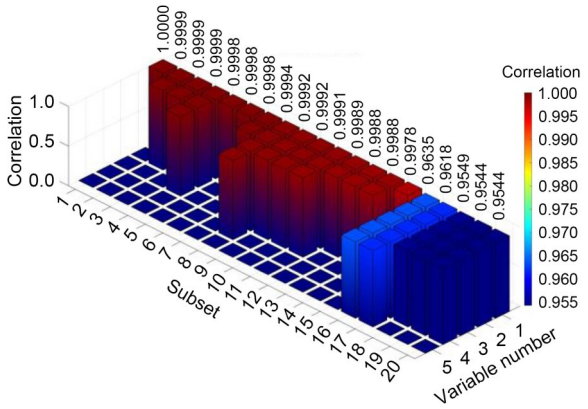


Fig. 2 Correlation heatmap based on the SCIM algorithm

correlation between each health feature subset and the SOH, with the intensity of the correlation indicated by color. The *X*-axis denotes the corresponding health feature subsets, while the *Y*-axis represents the number of variables in each respective health state subset. A correlation closer to 1 indicates a higher correlation. To obtain more variables, more health states are selected, comprising subset 2. The combination of charging energy and discharging capacity is chosen as the health feature subset.

For testing the LGRA algorithm, the discharging capacity, charging capacity, charging energy, charging DC internal resistance, and energy efficiency are defined as x_1–x_5 (Table 4). Based on the degree of correlation between each physical parameter and the SOH, the top 20 candidate subsets are filtered out and ranked in Table 5.

The correlations of the screening results are shown in Fig. 3, where the correlation between health feature subsets and SOH is also represented in the form of a heatmap. To obtain more variables in the LGRA algorithm, subset 4 (charging capacity, discharging capacity, and charging energy) is selected, because its correlation value is equivalent to that of subset 1 and it uses three variables rather than one. Since this study considers the interaction effects of multiple variables on the SOH, feature subsets with a larger number of

Table 4 Input variable by LGRA

Input variable	X
Discharging capacity	x_1
Charging capacity	x_2
Charging energy	x_3
Charging DC internal resistance	x_4
Energy efficiency	x_5

Table 5 Health feature subsets selected by LGRA

No.	Subset	No.	Subset
1	$\{x_1\}$	11	$\{x_2, x_3, x_4\}$
2	$\{x_1, x_2\}$	12	$\{x_1, x_4\}$
3	$\{x_1, x_3\}$	13	$\{x_2, x_4\}$
4	$\{x_1, x_2, x_3\}$	14	$\{x_3, x_4\}$
5	$\{x_2\}$	15	$\{x_4\}$
6	$\{x_2, x_3\}$	16	$\{x_1, x_2, x_3, x_4, x_5\}$
7	$\{x_3\}$	17	$\{x_1, x_2, x_3, x_5\}$
8	$\{x_1, x_2, x_3, x_4\}$	18	$\{x_1, x_2, x_4, x_5\}$
9	$\{x_1, x_2, x_4\}$	19	$\{x_1, x_3, x_4, x_5\}$
10	$\{x_1, x_3, x_4\}$	20	$\{x_2, x_3, x_4, x_5\}$

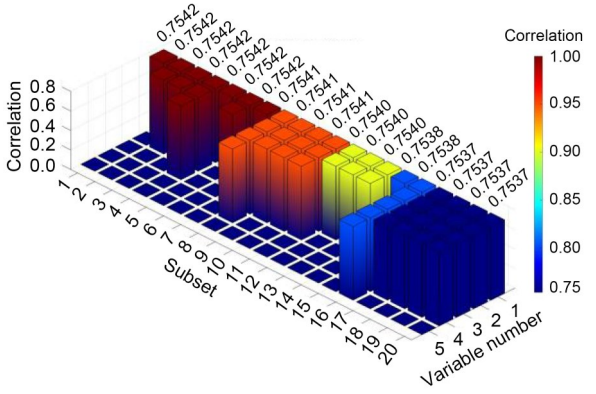


Fig. 3 Correlation heatmap based on the LGRA algorithm

variables are selected while ensuring that the correlation degree remains close to 1.

3.2 Optimal activation function based on LGRA

A comparative analysis of the feature subset selection capability of the LGRA and SCIM models for vanadium redox flow battery health indicators is conducted. The results show that LGRA outperforms SCIM. Therefore, LGRA is adopted as the feature selection method in this study. Detailed results are provided in the ESM.

Although the ELM architecture remains fixed, the choice of activation function significantly affects its performance. Based on the preceding analysis and discussion, LGRA is more suitable for predicting the SOH of VRFBs. Therefore, in the subsequent modeling process, the feature subset selected by LGRA is adopted as the input for SOH prediction to investigate the effects of different activation functions on SOH prediction.

Different activation functions yield markedly different results under the same parameter settings (Fig. 4). Moreover, even when using the same activation function, the predictive accuracy of ELM varies considerably depending on the swarm intelligence algorithm used. For instance, the sigmoid function shows strong performance when combined with PSO and SCSO but performs poorly with DBO and achieves the weakest results with ACO (Table 6).

Therefore, the main aim here is to identify the activation function that, when integrated with ELM, delivers the most stable and robust performance across various swarm intelligence optimization algorithms. As indicated by the preliminary screening results in Fig. 4, the tanh and sigmoid functions exhibit inconsistent behavior. In contrast, ELM models optimized with four different swarm intelligence algorithms consistently achieve superior predictive performance when using either the ReLU or linear activation functions.

To further investigate the effects of activation functions on prediction performance, a secondary analysis of data is conducted (Fig. 5). MAE, MSE, and MAPE are commonly used metrics to quantify prediction errors. Smaller values indicate higher prediction accuracy.

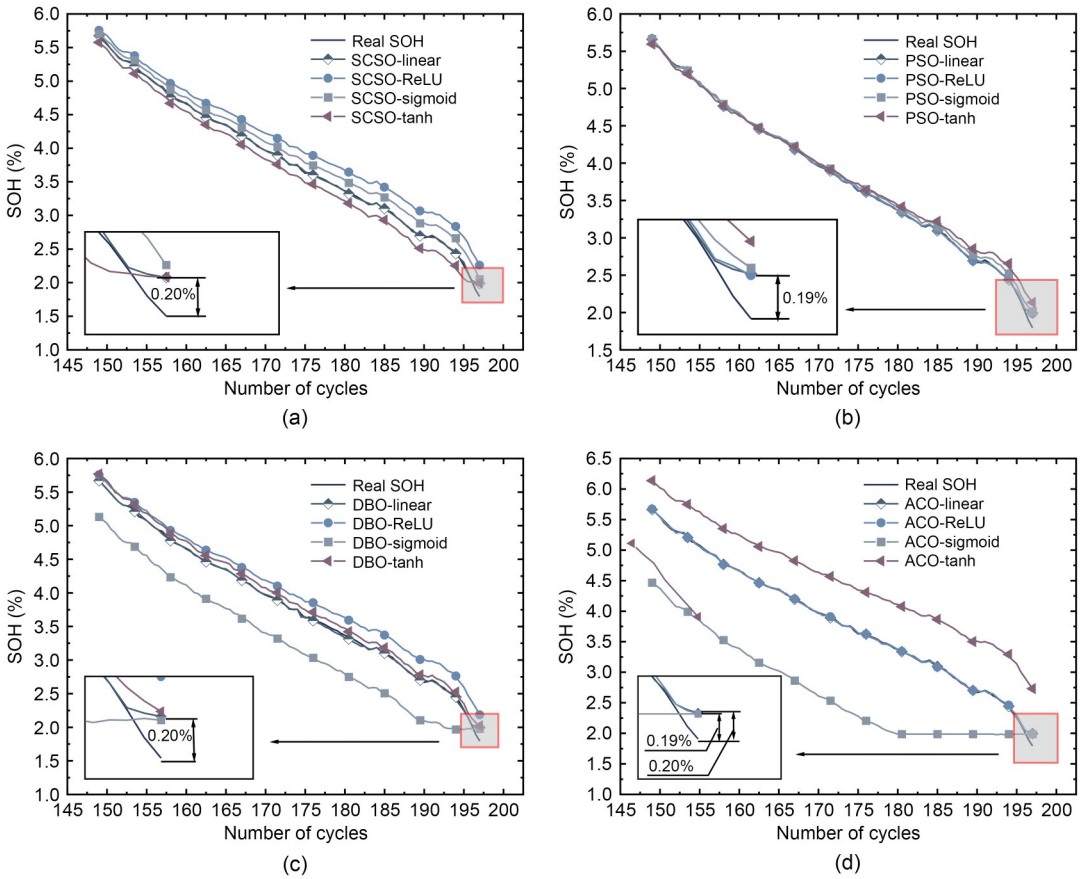


Fig. 4 SOH prediction results of different activation functions: (a) SCSO-ELM; (b) PSO-ELM; (c) DBO-ELM; (d) ACO-ELM

Table 6 SOH prediction situations of each model

Optimization algorithm	Activation function	SOH	
		Minimum difference	Maximum difference
SCSO	Linear	0.00006	0.19344
SCSO	ReLU	0.08219	0.47659
SCSO	Sigmoid	0.02767	0.29254
SCSO	tanh	0.01767	0.21894
PSO	Linear	0.00041	0.19725
PSO	ReLU	0.00001	0.19026
PSO	Sigmoid	0.00063	0.22230
PSO	tanh	0.00088	0.33948
DBO	Linear	0.00000	0.20024
DBO	ReLU	0.08431	0.39813
DBO	Sigmoid	0.04977	0.62903
DBO	tanh	0.05575	0.22475
ACO	Linear	0.00012	0.19928
ACO	ReLU	0.00022	0.19383
ACO	Sigmoid	0.04041	1.41036
ACO	tanh	0.46427	0.93467

Conversely, R^2 values closer to 1 signify better model performance.

When the linear activation function is used, the MAE values for PSO-ELM, SCSO-ELM, DBO-ELM, and ACO-ELM are 0.00717, 0.00782, 0.00805, and 0.02111, respectively, all near zero (Fig. 5). In contrast, when using the ReLU activation function, the MAE of SCSO-ELM and DBO-ELM increase substantially to 0.27276 and 0.22211, respectively, indicating lower prediction accuracy under this condition. Similarly, the MSE values for the four models with the linear activation function are close to zero, with the maximum MSE reaching only 0.00120. However, with ReLU activation, the highest MSE is 0.08132, followed by 0.05438, both significantly higher than those observed with linear activation. All four models using the linear activation function achieves R^2 values greater than 0.99, demonstrating excellent model fitting accuracy and overall superior predictive

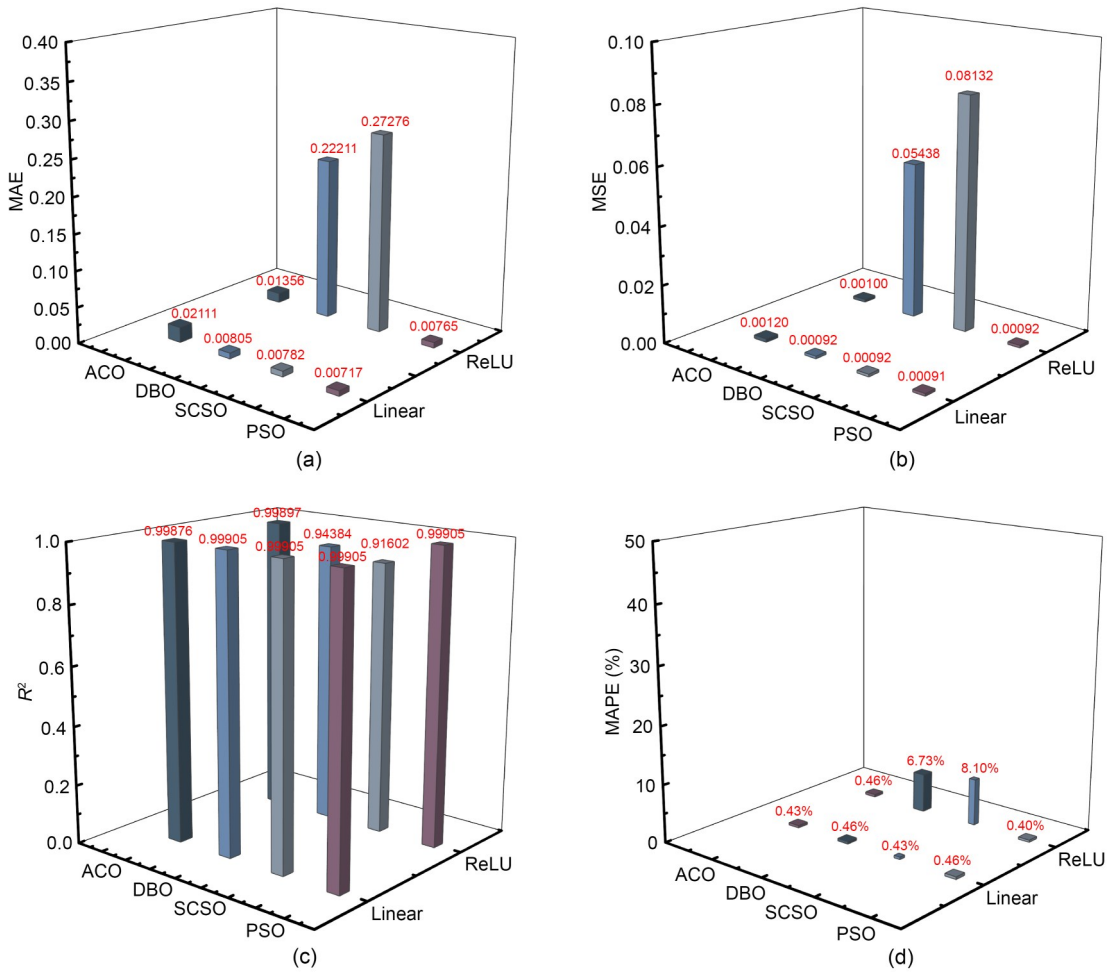


Fig. 5 ELM evaluation diagram based on four evaluation indicators: (a) MAE; (b) MSE; (c) R^2; (d) MAPE

performance compared to their ReLU counterparts. When evaluated by MAPE, the four models with linear activation show minimal errors ranging from 0.43% to 0.46%, whereas with ReLU activation, SCSO-ELM and DBO-ELM have considerably larger MAPE values of 8.10% and 6.73%, respectively. In conclusion, these results confirm that selecting the linear activation function for ELM results in the most stable and accurate model performance, particularly when combined with various swarm intelligence optimization algorithms.

3.3 Optimal swarm intelligence algorithm

Although ELM models can predict the SOH well, different swarm intelligence algorithms give different results. For SOH prediction, it is important to confirm the optimal or most suitable auxiliary intelligence algorithm. LGRA has been shown to be suitable for the prediction of flow battery SOH. Among the several activation functions of ELM, linear has the best performance. Therefore, the linear activation function and LGRA are used here. Fig. 6 illustrates the SOH prediction results of different swarm intelligence algorithms. The prediction performance of all four swarm intelligence algorithms is excellent, with a maximum error of only 0.2 percentage points (PPs). The prediction of the models not only shows high accuracy in numerical terms but also has a high degree of curve fitting, indicating that they can learn the decline characteristics and fluctuation of the real SOH.

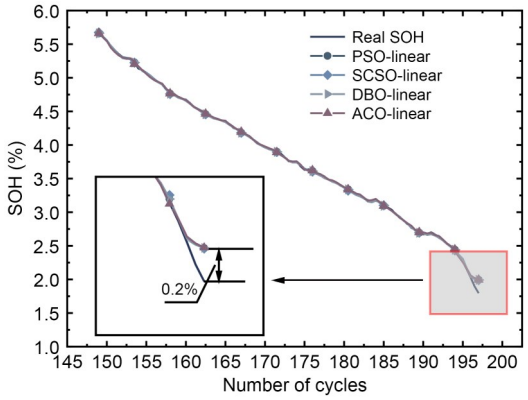


Fig. 6 SOH prediction results of different swarm intelligence algorithms

To compare the prediction results of the four swarm intelligence algorithms, further data analysis is carried out. Fig. 7 visualizes and quantifies the prediction performance of the model using four evaluation indicators. When PSO is used as the optimization algorithm, the MAE is 0.00717, the MSE is 0.00091, and the R^2 is 0.99905. These three metrics outperform those of the other three optimization algorithms, while the MAPE is 0.46%, only 0.03 PPs higher than the minimum MAPE observed.

PSO shows the best overall performance. It not only has low error but also an excellent fitting ability. Thus, we conclude that among the 32 algorithm models, LGRA-PSO-ELM-linear is the best.

To further investigate its effectiveness, a scatter plot of the predicted versus actual SOH values is presented in Fig. 8. The actual SOH values are plotted along the *X*-axis, while the corresponding predicted values are plotted along the *Y*-axis. The ideal prediction outcome corresponds to the 45° diagonal line (*Y*=*X*), representing perfect agreement between predicted

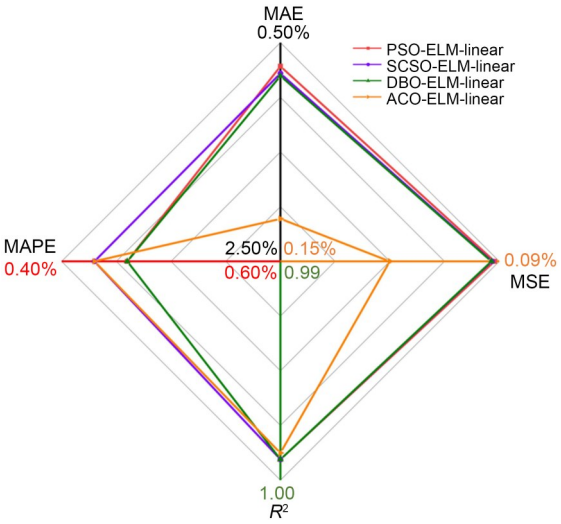


Fig. 7 Four evaluation indicators of ELM-linear models

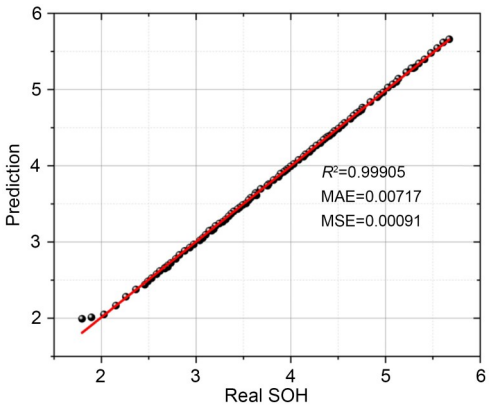


Fig. 8 Scatter plot of predicted and actual values of the LGRA-PSO-ELM-linear model

and actual values. Each black point in the figure represents a predicted SOH value. The closer these points are distributed around the $Y=X$ line, the smaller the prediction error, and the higher the model's accuracy. Moreover, the extent to which the distribution of black points aligns with the diagonal line reflects the model's ability to capture the actual SOH degradation trend. The dense and near-linear distribution of predicted values along this ideal line confirms the robustness and high fidelity of the LGRA-PSO-ELM-linear model in tracking SOH variations.

3.4 Different output features of ELM

Different subsets of output features are selected as inputs to the ELM model to verify the superiority of LGRA in feature selection. The LGRA algorithm identifies a feature subset consisting of the charging DC resistance and charging energy, with a correlation value of 0.7541. In the previous experiments, the selected feature subset composed of charging capacity, discharging capacity, and charging energy is referred to as subset 1, while the subset consisting of charging DC resistance and charging energy is denoted as subset 2 in this subsection. A comparative analysis is conducted between the two subsets under identical PSO and ELM parameter configurations.

Using the optimal activation function (linear) determined from the previous experiments, the model is executed three consecutive times to mitigate randomness and stochastic effects. The average of the three prediction results is adopted as the final evaluation metric. Fig. 9 shows that, despite the model being independently executed three times, the predicted SOH curves remain closely aligned with the actual SOH curve, showing only negligible variations. However, the prediction performance obtained with subset 2 is inferior to that of subset 1. Fig. 9c further presents the mean width of the 95% confidence interval corresponding to subset 1, demonstrating the high confidence level of the model and its strong stability, as indicated by the minimal fluctuations in output under repeated training or sample perturbations.

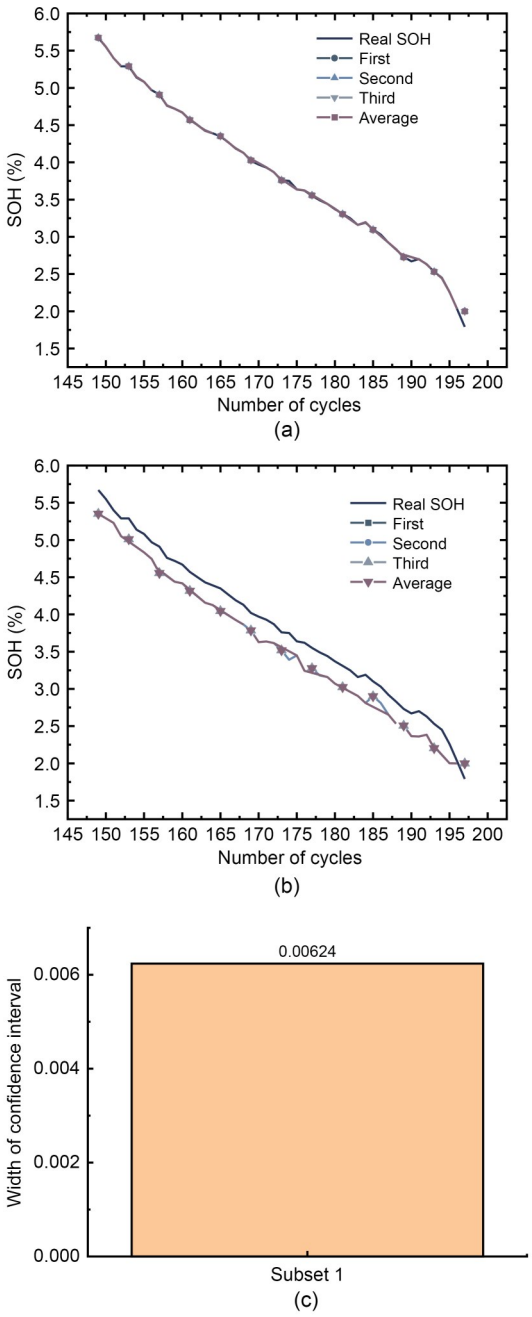


Fig. 9 Prediction results under different feature subsets: (a) subset 1; (b) subset 2; (c) average width of 95% confidence interval

3.5 Error fluctuation analysis across different cycle stages

The optimal model identified in the previous section is used to investigate the prediction error characteristics at different life stages. In the test dataset, the cycle number is used to represent the temporal sequence, and the entire test set is evenly divided into three stages by using one-third of the total number of test samples as the boundary for each stage. The corresponding error fluctuation characteristics are shown in Fig. 10. The prediction errors remain relatively low during the early and middle stages, while an increasing

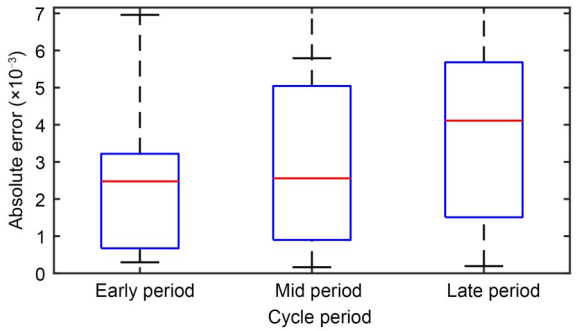


Fig. 10 Box plot of SOH prediction errors under different cycle periods

trend appears at the late stage. Nevertheless, the overall prediction accuracy is still well maintained.

3.6 Comparison of different prediction models

To investigate the prediction accuracy of different models optimized by the PSO algorithm for SOH estimation, we compare the performance of ELM and SVM models. Using identical PSO parameters, the hyperparameters of both ELM and SVM are optimized and their SOH prediction accuracies are compared under the same set of output features. The parameter settings of the PSO algorithm are listed in Table 7. The comparative results of ELM and SVM under the same PSO configurations are shown in Fig. 11. The performance of ELM significantly surpasses that of SVM, and the computational time of ELM is substantially shorter. These results indicate that, under conditions of limited sample size and iteration count, ELM exhibits markedly superior computational efficiency and prediction accuracy compared to SVM.

Table 7 PSO parameter settings

Parameter	Value
Number of particles, N_p	10
Maximum number of iterations, T_{max}	50
Inertia weight, w	0.8
Cognitive learning factor, c_1	1.5
Social learning factor, c_2	1.5

3.7 Robustness of the model under noisy data

In the process of SOH modeling of redox flow batteries, experimental data are inevitably affected by both measurement noise and operational disturbances. To more realistically evaluate the generalization capability of the proposed model under practical engineering scenarios, a composite noise structure consisting

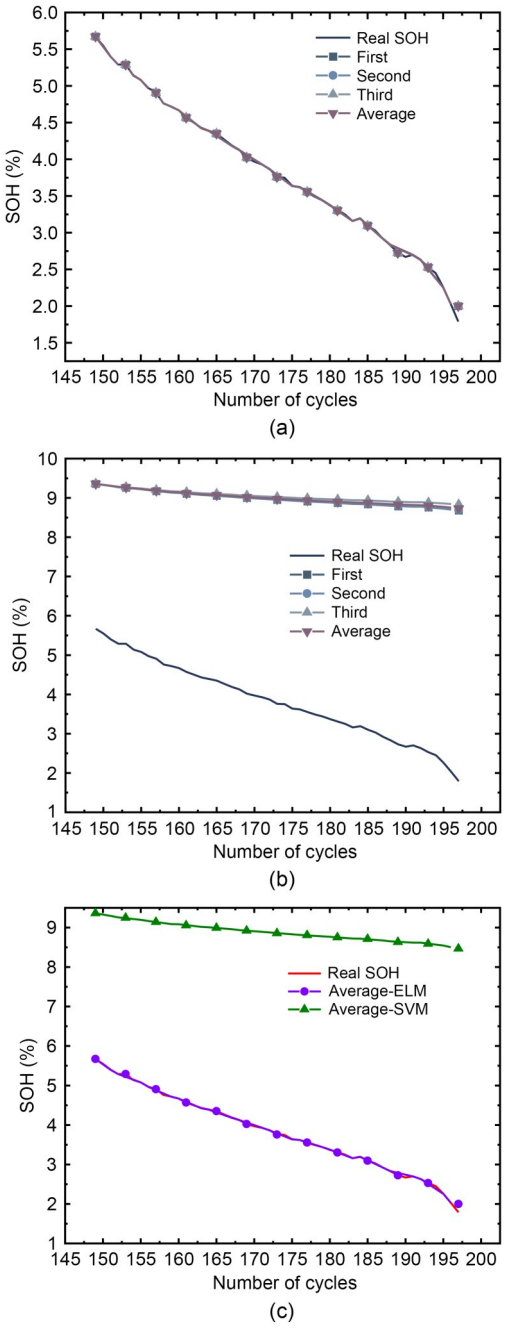


Fig. 11 Comparison of prediction effects between ELM and SVM: (a) predictive performance of ELM; (b) predictive performance of SVM; (c) comparison of the average predicted values of ELM and SVM

of Gaussian white noise and bounded abnormal perturbations is introduced at the feature level of the original dataset, thereby emulating the data uncertainty encountered during long-term operation of real flow battery systems.

First, Gaussian white noise is used to simulate random measurement errors introduced by sensors

monitoring voltage, current, temperature, and other operational variables in practical experiments. The noise intensity is set to 0.2% of the normalized feature magnitude, which is consistent with the typical accuracy range of laboratory-grade data acquisition systems. This noise level does not significantly distort the statistical distribution of the original signals, while effectively assessing the robustness of the model against small-amplitude random disturbances. Owing to its zero-mean and independent identically distributed characteristics, Gaussian white noise does not carry systematic degradation information, but purely represents measurement uncertainty, thereby imposing more stringent requirements on model stability.

Furthermore, to better approximate the complex operating conditions encountered in real flow battery applications, a small proportion of bounded abnormal perturbation points is also incorporated. The proportion of such perturbations is set to 1%, with the disturbance amplitude constrained within ±5%, aiming to emulate non-ideal operating events such as pump speed fluctuations, transient instability of electrolyte flow rate, and abrupt electrochemical polarization variations. Unlike conventional extreme outliers, these perturbations are strictly bounded in magnitude and further constrained by normalization-based clipping, ensuring that all features remain within physically feasible ranges and avoiding the introduction of non-physical data contamination. This design is more representative of the "weak anomalies under strong constraints" commonly observed in engineering practice.

Note that noise is introduced exclusively at the input feature level, while the SOH labels are kept unchanged. This treatment is motivated by the physical nature of SOH evolution in flow batteries, which is inherently gradual and reflects long-term degradation processes rather than instantaneous operational fluctuations. Consequently, measurement noise predominantly affects observable operational features rather than the health state. This strategy preserves the physical consistency of the learning objective and prevents error propagation caused by artificially induced label noise.

Under the specified noisy conditions, the PSO-ELM model using a linear activation function shows superior prediction accuracy and stability. This indicates that, after prior feature selection and normalization, the input variables are already capable of effectively capturing the dominant degradation mechanisms governing SOH evolution. Introducing additional nonlinear mappings may instead amplify random noise and abnormal perturbations, leading to overfitting to local disturbances. In contrast, linear activation functions inherently provide a noise-averaging effect in high-dimensional feature spaces, suppressing the influence of unstructured disturbances on model outputs and resulting in a smoother and more stable PSO optimization process.

In summary, the introduced noise is not designed to artificially enhance model performance, but rather to construct a realistic disturbance scenario grounded in actual flow battery operating environments. The superior performance of the PSO-ELM-linear model under these conditions further validates the effectiveness of the selected feature set in characterizing SOH degradation mechanisms. Moreover, it shows that, in uncertainty-dominated environments, an appropriately constrained model complexity is more conducive to achieving robust and reliable health state prediction. The prediction results of different models under noisy conditions and the corresponding noise configurations are shown in Fig. 12 and Table 8.

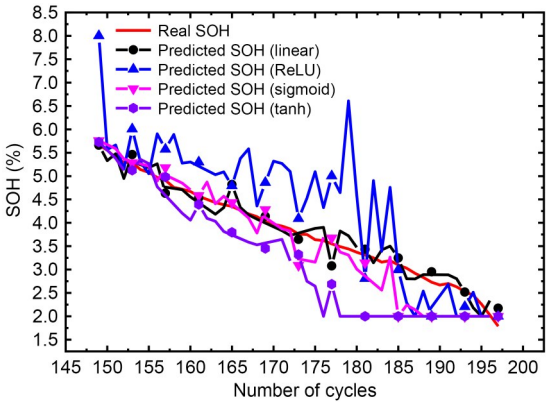


Fig. 12 Phenotypic characteristics of models with different activation functions under noisy data

Table 8 Specific configuration of noisy data

Noise type	Mathematical formulation	Disturbance ratio
Gaussian white noise	$x'=x+\sigma N(0, 1)$	0.2%
Bounded perturbation	$x'=x+\delta$, $\delta\in[-5\%, 5\%]$	1% of samples
Physical constraint clipping	$x'\in[0, 1]$	

x and x' denote the original and perturbed data, respectively. σ is the standard deviation of Gaussian noise, $N(0, 1)$ represents a standard normal distribution, and δ is a bounded perturbation term within a predefined range

4 Conclusions

In this study, an SOH estimating model is established based on an ELM and swarm intelligence algorithm. A series of charging/discharging cycle tests is conducted, and eight operating parameters are extracted as health feature subsets, which are selected by the SCIM and LGRA algorithms. The Spearman's correlation coefficient and gray relation coefficient are used to evaluate and select the optimal health feature subsets, identifying charging capacity, discharging capacity, and charging energy as health feature subsets. The effects of different swarm intelligence algorithms and different activation functions on SOH estimation performance are studied based on 32 prediction models. The results show that the sigmoid activation function is incapable of predicting SOH because all models using that function have poor prediction performance. The most suitable swarm intelligence algorithm is PSO, and the best activation function is linear, which has a maximum error lower than 0.2%. The superiority of LGRA and ELM is further confirmed by comparing different models and input features. Furthermore, robustness tests are conducted for different models by simulating noisy environments, and the above conclusions remain valid.

Acknowledgments

This work is supported by the National Natural Science Foundation of China (No. 52476050) and the Beijing Natural Science Foundation of China (No. 3232025).

Author contributions

Fengming CHU designed the research. Zebo HUANG processed the corresponding data. Lei ZHANG drafted the paper. Guo'an YANG helped organize the paper. Fengming CHU revised and edited the final version.

Conflict of interest

Lei ZHANG, Zebo HUANG, Guo'an YANG, and Fengming CHU declare that they have no conflict of interest.

Declaration on the use of generative AI tools

No generative AI tools were used in the preparation of this manuscript.

Data availability

The data that support the findings of this study are available from the corresponding author upon reasonable request.

References

Calborean A, Bruj O, Murariu T, et al., 2020. Resonance frequency analysis of lead-acid cells: an EIS approach to predict the state-of-health. *Journal of Energy Storage*, 27: 101143. https://doi.org/10.1016/j.est.2019.101143

Chang C, Wang QY, Jiang JC, et al., 2021. Lithium-ion battery state of health estimation using the incremental capacity and wavelet neural networks with genetic algorithm. *Journal of Energy Storage*, 38:102570. https://doi.org/10.1016/j.est.2021.102570

Chen K, Li JL, Liu K, et al., 2024. State of health estimation for lithium-ion battery based on particle swarm optimization algorithm and extreme learning machine. *Green Energy and Intelligent Transportation*, 3(1):100151. https://doi.org/10.1016/j.geits.2024.100151

Chu FM, Wang YZ, Liu X, et al., 2026. Optimization of porous electrode configuration for organic redox flow battery by machine learning based on back propagation neural network based on firefly. *Journal of Energy Storage*, 148:120052. https://doi.org/10.1016/j.est.2025.120052

Feng RJ, Guo ZS, Meng X, et al., 2025. Modeling and state of charge estimation of vanadium redox flow batteries: a review. *Energies*, 18(17):4666. https://doi.org/10.3390/en18174666

Ge MF, Liu YB, Jiang XX, et al., 2021. A review on state of health estimations and remaining useful life prognostics of lithium-ion batteries. *Measurement*, 174:109057. https://doi.org/10.1016/j.measurement.2021.109057

Gong JQ, Xu B, Chen FH, et al., 2025. Predictive modeling for electric vehicle battery state of health: a comprehensive literature review. *Energies*, 18(2):337. https://doi.org/10.3390/en18020337

Gu XB, Huan X, Ren Y, et al., 2026. Real-time physics-aware battery health monitoring from partial charging profiles via physics-informed neural networks. *eTransportation*, 28:100555. https://doi.org/10.1016/j.etran.2026.100555

Guo ZX, Sun J, Wang ZY, et al., 2023. Numerical modeling of interdigitated flow fields for scaled-up redox flow batteries. *International Journal of Heat and Mass Transfer*, 201:123548. https://doi.org/10.1016/j.ijheatmasstransfer.2022.123548

Huang R, Fogelquist J, Lin XF, 2025. Robust estimation of battery state of health using reference voltage trajectory. American Control Conference, p.4065-4070. https://doi.org/10.23919/acc63710.2025.11108071

Lei X, Xie FJ, Wang JL, et al., 2024. A review of lithium-ion battery state of health and remaining useful life estimation methods based on bibliometric analysis. *Journal of Traffic and Transportation Engineering (English Edition)*, 11(6):1420-1446. https://doi.org/10.1016/j.jtte.2024.09.004

Li J, Adewuyi K, Lotfi N, et al., 2018. A single particle model with chemical/mechanical degradation physics for lithium ion battery state of health (SOH) estimation. *Applied*

Energy, 212:1178-1190.
https://doi.org/10.1016/j.apenergy.2018.01.011

Li PH, Zhang ZJ, Xiong QY, et al., 2020. State-of-health estimation and remaining useful life prediction for the lithium-ion battery based on a variant long short term memory neural network. *Journal of Power Sources*, 459:228069.
https://doi.org/10.1016/j.jpowsour.2020.228069

Li S, Li K, Xiao E, et al., 2020. Joint SoC and SoH estimation for zinc–nickel single-flow batteries. *IEEE Transactions on Industrial Electronics*, 67(10):8484-8494.
https://doi.org/10.1109/TIE.2019.2949534

Lin CS, Tuo X, Wu LX, et al., 2025. Physics-informed machine learning for accurate SOH estimation of lithium-ion batteries considering various temperatures and operating conditions. *Energy*, 318:134937.
https://doi.org/10.1016/j.energy.2025.134937

Meng JH, Cai L, Luo GZ, et al., 2018. Lithium-ion battery state of health estimation with short-term current pulse test and support vector machine. *Microelectronics Reliability*, 88-90:1216-1220.
https://doi.org/10.1016/j.microrel.2018.07.025

Meng X, Sun CY, Mei J, et al., 2025a. Fuel cell life prediction considering the recovery phenomenon of reversible voltage loss. *Journal of Power Sources*, 625:235634.
https://doi.org/10.1016/j.jpowsour.2024.235634

Meng X, Liu MJ, Mei J, et al., 2025b. Polarization loss decomposition-based online health state estimation for proton exchange membrane fuel cells. *International Journal of Hydrogen Energy*, 157:150162.
https://doi.org/10.1016/j.ijhydene.2025.150162

Patil MA, Tagade P, Hariharan KS, et al., 2015. A novel multistage support vector machine based approach for Li ion battery remaining useful life estimation. *Applied Energy*, 159:285-297.
https://doi.org/10.1016/j.apenergy.2015.08.119

Ren JY, Wei L, Wang ZY, et al., 2022. An electrochemical-thermal coupled model for aqueous redox flow batteries. *International Journal of Heat and Mass Transfer*, 192: 122926.
https://doi.org/10.1016/j.ijheatmasstransfer.2022.122926

Shen S, Sadoughi M, Chen XY, et al., 2019. A deep learning method for online capacity estimation of lithium-ion batteries. *Journal of Energy Storage*, 25:100817.
https://doi.org/10.1016/j.est.2019.100817

Struckmann T, Kuhn P, Ressel S, 2020. A combined in situ monitoring approach for half cell state of charge and state of health of vanadium redox flow batteries. *Electrochimica Acta*, 362:137174.
https://doi.org/10.1016/j.electacta.2020.137174

Sui X, He S, Vilsen SB, et al., 2021. A review of non-probabilistic machine learning-based state of health estimation techniques for lithium-ion battery. *Applied Energy*, 300: 117346.
https://doi.org/10.1016/j.apenergy.2021.117346

Sun GQ, Liu YF, Liu XW, 2025. RETRACTED: a method for estimating lithium-ion battery state of health based on physics-informed machine learning. *Journal of Power Sources*, 627:235767.
https://doi.org/10.1016/j.jpowsour.2024.235767

Tan P, Chen B, Xu HR, et al., 2017. Flexible Zn– and Li–air batteries: recent advances, challenges, and future perspectives. *Energy & Environmental Science*, 10(10):2056-2080.
https://doi.org/10.1039/C7EE01913K

Wang FJ, Wu ZQ, Zhao ZB, et al., 2024. Physical knowledge guided state of health estimation of lithium-ion battery with limited segment data. *Reliability Engineering & System Safety*, 251:110325.
https://doi.org/10.1016/j.ress.2024.110325

Wang LM, Zhao XL, Liu L, et al., 2017. State of health estimation of battery modules via differential voltage analysis with local data symmetry method. *Electrochimica Acta*, 256:81-89.
https://doi.org/10.1016/j.electacta.2017.10.025

Wei ZB, Xiong R, Lim TM, et al., 2018. Online monitoring of state of charge and capacity loss for vanadium redox flow battery based on autoregressive exogenous modeling. *Journal of Power Sources*, 402:252-262.
https://doi.org/10.1016/j.jpowsour.2018.09.028

Yao L, Xu SM, Tang AH, et al., 2021. A review of lithium-ion battery state of health estimation and prediction methods. *World Electric Vehicle Journal*, 12(3):113.
https://doi.org/10.3390/wevj12030113

Yu WT, Shang WX, He Y, et al., 2022. Unraveling the mechanism of non-uniform zinc deposition in rechargeable zinc-based batteries with vertical orientation. *Chemical Engineering Journal*, 431:134032.
https://doi.org/10.1016/j.cej.2021.134032

Zhang SZ, Zhai BY, Guo X, et al., 2019. Synchronous estimation of state of health and remaining useful lifetime for lithium-ion battery using the incremental capacity and artificial neural networks. *Journal of Energy Storage*, 26: 100951.
https://doi.org/10.1016/j.est.2019.100951

Zhao JH, Zhu Y, Zhang B, et al., 2023. Review of state estimation and remaining useful life prediction methods for lithium–ion batteries. *Sustainability*, 15(6):5014.
https://doi.org/10.3390/su15065014

Electronic supplementary materials

Sections S1–S4, Table S1, Figs. S1–S8, Eqs. (S1)–(S6)